DEM-Simulation of the Magnetic Field Enhanced Cake Filtration

Christian Eichholz and Hermann Nirschl
Institute of Mechanical Engineering and Mechanics, Karlsruhe Institute of Technology, Karlsruhe, Germany

Fei Chen and T. Alan Hatton
Dept. of Chemical Engineering, Massachusetts Institute of Technology, Cambridge, MA 02139

DOI 10.1002/aic.13759
Published online February 16, 2012 in Wiley Online Library (wileyonlinelibrary.com).

Using the discrete element method, we simulate numerically the cake formation and growth in magnetic field enhanced cake filtration to give further insight on the mechanisms of the structuring of the filter cake due to the interaction of magnetic, hydrodynamic, and mass forces. The motion of the discrete particles is obtained by applying the three-dimensional Newton's equations to individual particles, allowing for both external forces (gravity, applied magnetic field) and particle–particle interactions calculated using the modified DLVO-theory. Continuous liquid phase flow is assumed as one-dimensional. The simulation results compare favorably with reported experimental data,[1] and can be used to delineate the regimes associated with different liquid flow and magnetic field effects that are observed experimentally.
 AIChE J, 58: 3633–3644, 2012
Keywords: discrete element method, simulation, magnetic filtration, magnetic fields, magnetic particles

Introduction

Cake filtration is a classic unit operation applied widely to the separation and processing of particulate systems.[2] Extensive investigations, both experimental and theoretical, have led to a detailed understanding of the filtration process, in which the particles are retained by a filter medium while the liquid phase passes through the filter due to a differential pressure drop across the filter. In the early stages of the process, the particles are held back by the filter medium itself, but as the filter cake builds up with time, it becomes the dominant particle retention matrix. The filter cake provides a resistance to the filtrate flow that increases with increasing filtration time and cake height, and results in a decrease in filtration rate with time. This is especially true for fine grained or compressible materials, where this resistance can limit the application range of filtration processes. Clearly, significant enhancements in processing rates could accrue if the rate of cake formation and the structure of the cake itself were to be optimized.

Magnetic field enhanced cake filtration, which combines the advantages of classical cake filtration and magnetic field driven separations, has been proposed as an effective means for the boosting of filtration process rates.[1,3] This operation exploits the forces experienced by magnetic particles subjected to an inhomogeneous magnetic field when in a direction opposite that of the differential pressure drop driving the fluid phase through the filter, effectively providing a partial decoupling of the solid and liquid phase motions. This partial decoupling of movement leads to slower cake formation, and thus a smaller filtration resistance to the liquid permeating through the filter cake. At high field strengths, the cake build-up can even be prevented, as the filter medium can be kept free of particles and the filtrate can drain through the filter medium almost without resistance. The magnetic forces not only influence the rate of cake built-up but also have an impact on the structure of the filter cake. When exposed to a magnetic field, the particles become magnetized and act as microscopic magnets themselves. The resulting interparticle forces lead to an alignment of the particles and formation of agglomerates in the direction of the external magnetic field.[4,5] The permeability of a cake with this channeled structure is higher than that of a filter cake in conventional filtration operations.

Experimental results prove that these different magnetic field effects influence the filtration process positively, especially for ferro- and superparamagnetic materials. Magnetic field enhanced cake filtration is not restricted to a single procedural principle in cake filtration, and has, to date, been implemented successfully in a filter press[6] and a nutsche filter,[1,3] and this separation concept has more recently been demonstrated to be effective also in continuous processing using a magnetic drum filter.[7]

Further insights into these processes are needed to guide the development of new configurations and the scale-up of the existing concepts. These insights can be gained through appropriate modeling of the particle–particle interactions, as mediated by the flow and magnetic fields, using the discrete element method (DEM) first developed by Cundall and Strack.[8] This approach for the description of granular

Correspondence concerning this article should be addressed to C. Eichholz at this current address: Process Research and Chemical Engineering, BASF SE, Ludwigshafen, Germany; e-mail: christian.eichholz@basf.com.
Current address of F. Chen: Air Products and Chemicals Inc., PA.

materials has many features in common with the molecular dynamic methods used to describe time-dependent physical processes on the atomic or molecular scale, e.g., in chemistry or thermodynamics.[9] The basic principle of DEM is to solve Newton's laws of motion for all discrete elements in the system, allowing for all degrees of freedom and considering all forces acting on the particles, to describe the motion of each particle individually. The original work of Cundall and Strack considered the stress on the granular media generated by external forces, and friction or elastic impacts between two spheres, but did not account for intermolecular or interparticle forces. More recently, particle interactions have also been included for fine particulate systems on the micrometer scale.[10–12] Dong especially worked on the cake build-up mechanisms in filtration and sedimentation.[12] They could demonstrate the influence of material properties on the cake structure and the contact force network inside the filter cake or sediment.

In general, the forces acting on the particles can be categorized as either primary or secondary forces. Primary forces are those due to external effects and interparticle interactions occurring in the system (compare Section *Forces on Particles*), while secondary, contact forces are those associated with the actual strains within the interparticle contact regions (compare section *Contact Forces*).

Focusing on the comparison of experimental and simulated results we have used the DEM method in this article to probe the effects of applied magnetic fields on cake formation and growth in magnetic field enhanced cake filtration processes. The results, which compare favorably with experimentally observed behavior, emphasize structure development within the cakes, as reflected in the cake height, porosity, and tortuosity, and their influence on the filter cake resistance and filtration rates with time.

Magnetic Field Enhanced Cake Filtration

Basic principles

As noted above, magnetic field enhanced cake filtration exploits the combination of classical cake filtration and magnetic separation to decouple partially the solid and liquid phase motions. When the magnetic and hydrodynamic forces on the particles act in opposite directions, the rate at which the particles are swept toward the filter is reduced, and hence so is the rate of deposition of these particles on or within the cake, and the cake formation proceeds at a much slower rate. Consequently, the packed bed through which the liquid phase must drain is of lower height, and offers a smaller filtration resistance than it would in the absence of the magnetic field. If the magnetic field is sufficiently strong, above a critical magnetic flux density B_{crit}, it is even possible to prevent the formation of the cake at the beginning of the filtration process such that the filter medium is kept free of particles, and the filtrate can pass through the filter medium almost without resistance. In batch processes, only after the removal of the excess water fed to the filter do the particles deposit on the filter medium.

In addition to its effect on the rate of cake build-up, the magnetic force can also impact the structure of the filter cake, depending on the magnetic field strength. When exposed to the magnetic field, the particles become magnetized and align with the external field. The resulting interparticle forces between approaching particles lead to the formation of chainlike agglomerates in the direction of the external magnetic field, while particles orientated perpendicular to the field direction experience a repulsive force.[4,5] The permeability of a cake with this channeled structure is higher than that of a filter cake obtained in classical filtration runs. Together, these two effects result in a reduction of the filtration resistance and thus in a strong improvement of filtration kinetics. Experimental results prove that these different magnetic field effects influence the filtration process positively, especially for ferro- and superparamagnetic materials.[1,3,6,7]

The modeling work presented here is complementary to the experimental investigations of magnetic field enhanced cake filtration using superparamagnetic particles in a lab-scale Nutsche filter.[1] The filter cell itself was placed in the bore of a solenoid, and constructed of nonmagnetic materials not to influence the applied magnetic field. The electro magnet had a maximum field strength of 0.4T, and an iron frame distorted the magnetic field inside the bore to increase the magnetic flux density gradient. The filter cell was located below the horizontal center of the solenoid such that the highest magnetic force density $B \cdot \nabla B$ occurred in the region of the filter medium. In this position, the magnetic and hydrodynamic drag forces acted in opposite directions.

Forces on particles

The primary forces acting on the particles can be divided into (i) external forces, which act on individual particles depending on their absolute position in the apparatus or simulation area, and (ii) interaction forces between neighboring particles.

External forces

In the processes considered here, the external forces acting on a particle with diameter d are due to gravity, buoyancy, hydrodynamic, and external magnetic field effects. The gravity and buoyancy forces $F_{\mathrm{b,g}}$, captured by the equation

$$\vec{F}_{\mathrm{g,b}} = \frac{\pi}{6} d^3 \Delta\rho_{\mathrm{sl}} \vec{g}, \tag{1}$$

with the density difference $\Delta\rho_{\mathrm{sl}}$ between the solid and the liquid phase and the gravitational acceleration g, play only a minor role in the processes of interest because generally they are much smaller than the other forces in the system.

A detailed analysis of the hydrodynamic conditions and hydrodynamic particle interactions is complex[13,14] and beyond the scope of this work. In this study, the hydrodynamic force F_{hyd} was assumed to be proportional to the relative velocity between the filtrate (v_∞) and the particles (v) and the dynamic viscosity η in accord with Stokes' law, given by

$$\vec{F}_{\mathrm{hyd}} = 3\pi\eta d(\vec{v}_\infty - \vec{v}) \tag{2}$$

In filtration processes this assumption is valid for low filtration velocities, i.e., low Reynolds numbers, and low solid concentrations in the suspension.

The magnetic force $F_{\mathrm{m,ext}}$ is a function of the gradient of the magnetic flux density ∇B, which itself depends on the position in the external magnetic field, and the magnetization of the particles themselves, and is given by the equation

$$\vec{F}_{\mathrm{m,ext}} = \frac{\pi}{6} d^3 \rho_{\mathrm{s}} M \cdot \nabla B \tag{3}$$

Material properties are reflected in the particle density ρ_s and the magnetization M; the latter is a function of the atomic magnetic moments and the applied magnetic field strength.

Interparticle forces

Usually, the forces between particles in a liquid phase are described by the DLVO-theory,[15,16] which accounts for the effects of electrostatic repulsion, van der Waals attraction and Born repulsion. This analysis has recently been extended to magnetized systems by accounting also for magnetic particle interactions.[5,17,18] The principle concept of the DLVO-theory—the reduction of a system to consider only binary particle interactions—makes it suitable for describing the interparticulate forces in DEM-simulations.

In the liquid phase, electrostatic repulsion is due to the surface charge on dispersed particles that can arise due to, e.g., proteolysis, ionic adsorption, or dissociation. For particles of the same material, Gregory[19] suggested the approximation to the repulsive interaction force $F_{el,ij}$ between unequal sized spheres given by

$$\vec{F}_{el,ij} = \frac{128\pi N_A c_{Ion} kT}{\kappa^2}\left(\frac{d_i d_j}{4}\right)\gamma_i\gamma_j\left(\frac{1}{r_{ij}^2}-\frac{\kappa}{r_{ij}}\right) \times \exp\left\{-\kappa\left(r_{ij}-\frac{d_i+d_j}{2}\right)\right\}\vec{n}_{ij}$$

$$\text{with} \quad \frac{1}{\kappa}=\lambda_D=\sqrt{\frac{\varepsilon_r\varepsilon_0 kT}{e_0^2 N_A \sum z_{Ion}^2 c_{Ion}}} \quad \text{and} \quad \gamma_i=\frac{\exp\left\{\frac{z_{Ion}e_0\zeta_i}{2kT}\right\}-1}{\exp\left\{\frac{z_{Ion}e_0\zeta_i}{2kT}\right\}+1} \tag{4}$$

with the the Avogadro number N_A, the elementary charge e_0, the Boltzmann constant k, the temperature T, the ion concentration c_{Ion}, the valence number z_{Ion}, the reciprocal Debye length κ, the center-to-center distance r_{ij} of the two particles and the center vector $\vec{n}$ between the two particles.

The Debye length λ_D depends strongly on the ionic strength of the liquid phase and is the distance from the particle surface over which the electrostatic potential decreases by a factor of 1/e. The surface charge itself is approximated by the zeta potential ζ, which depends on the pH of the suspension.

The attractive van der Waals force originates from the movement of the electrons in the atomic shell causing a shift in the atomic charge distribution to give instantaneous electronic dipoles that interact with each other.[20] The resulting force $F_{vdW,ij}$ between two spherical particles with different diameters can be calculated from

$$\vec{F}_{vdW,ij} = -\frac{H_0}{6} r_{ij} d_i d_j \left\{\left[r_{ij}^2-\left(\frac{d_i+d_j}{2}\right)^2\right]^{-1} - \left[r_{ij}^2-\left(\frac{d_i-d_j}{2}\right)^2\right]^{-1}\right\}^2 \vec{n}_{ij} \tag{5}$$

where H_0, the Hamaker constant, accounts for the material properties of both the particles and the intervening solvent phase, and can be calculated from the values for the pure components. Available data indicate that H_0 can vary over the range 0.3×10^{-20} to 1.4×10^{-20} J for polymer materials in water.[21]

Short range or Born repulsion is represented by defining a theoretical minimum distance a_0 between the two surfaces at which the repulsive forces overcome completely any attractive forces that might exist at that position. This approach also circumvents the singularity problem of the van der Waals force that arises on direct particle–particle contact. This minimum distance differs tremendously from case to case, by as much as two decades in magnitude.[12,13,22] Clearly, the two parameters H_0 and a_0 must be determined carefully since the entire force balance over the interacting particles is very sensitive to the absolute value of the van der Waals force. For our simulation, the parameters adopted are those used in Refs. 21 and 12.

The magnetic dipole force $F_{m,dip,ij}$ acts over a relatively large distance compared to the ranges of the other interparticle forces. It depends on the magnitudes and directions of the magnetic moments of both particles,[23] each of which is generally taken to be the average over all magnetic domains within the individual particle volumes, and assumed to align with the external field. The particles attract and align in the field direction but experience a repulsive force perpendicular to this direction, as captured in the equation given in Refs. 24 and 25:

$$\vec{F}_{m,dip,ij} = -\frac{3\pi\mu_0\rho_s^2 d_i^3 d_j^3}{144}\left(\frac{M_i M_j}{r_{ij}^4}\right)\Big[-\langle\vec{m}_i\cdot\vec{m}_j\rangle\vec{n}_{ij}+5\langle\vec{m}_i\cdot\vec{n}_{ij}\rangle \times\langle\vec{m}_j\cdot\vec{n}_{ij}\rangle\vec{n}_{ij}-\langle\vec{m}_j\cdot\vec{n}_{ij}\rangle\vec{m}_i-\langle\vec{m}_i\cdot\vec{n}_{ij}\rangle\vec{m}_j\Big] \tag{6}$$

The norm of the magnetic dipole force depends on the size of the particles, their actual magnetizations M_i and M_j (which depend on the magnetic field strength), the magnetic permeability constant μ_0 and the center distance r_{ij}. The direction of the force is determined by the relative orientations of the magnetic moments $\vec{m}_i$ and $\vec{m}_j$, which we assume to be aligned with the strong external magnetic fields considered in this work.

This equation for the magnetic dipole force describes the interaction between two homogeneous magnetized particles. This approach overestimates the influence of the dipole interactions in composite particles simulated in this work. Mainly, this is due to the low range of influence of a single magnetic seed within the composite particles. Therefore, an effective magnetization is introduced to account for the reduced field deformation or reduced local field gradient within the beads. Investigations with a new magnetic analyzing centrifuge show an effective magnetization $M_{eff} = 0.39\,M$ for the present PVAc particle system.[7] M accounts for the averaged magnetization of the PVAc particle, which is considered for calculating the external magnetic force (Eq. 3).

Permeation of a packed bed in the magnetic field enhanced cake filtration

The filtrate velocity v_∞ is proportional to the applied differential pressure Δp, and decreases with time because of the increasing resistance offered by the filter cake comprised of the deposited particles. This velocity can be calculated using Ruth's law[26] coupled with the Karman–Cozeny relation for the permeability P_c of filter cakes[27]:

$$v_\infty = \frac{\Delta p}{\eta\left(R_m+\frac{h_c}{P_c}\right)} \tag{7}$$

$$P_c = \frac{1}{r_c} = \frac{d^2}{36k_0\tau^2}\left(\frac{\varepsilon^3}{(1-\varepsilon)^2}\right) \tag{8}$$

$$\tau = \frac{h_{\mathrm{eff}}}{h_{\mathrm{c}}} \tag{9}$$

The change in the permeability of the filter cake (Eq. 8) or its specific filtration resistance r_{c} due to the superposed magnetic field is reflected in changes in both the porosity ε and tortuosity τ (Eq. 9). Further, the constant k_0 accounts for the influence of the pore geometry. The tortuosity, calculated as the ratio of the effective capillary length through the filter cake h_{eff} to its height h_{c}, is an indicator of the geometry of the capillary system; the smaller is τ the more direct is the channel through the cake. For a τ value of unity, the pores pass straight through the bed with no bends.

Ruth's law reflects the dependency of the ratio of filtration time t to filtrate volume V on the process parameters and material properties. It has been shown that Ruth's law can be extended to magnetic field enhanced cake filtration[1,3] in which changes in the cake structure due to the magnetic field are reflected in changes to the filter cake resistance. The impact of the external magnetic field gradient on the rate of cake build-up is described by the magnetophoretic coefficient, which is a measure of the relative approach of the actual magnetic force to the critical force (index in eq.10: crit), or equivalent magnetic flux density, at which no cake build-up occurs, because the external magnetic force exceeds the remaining forces. These effects can be accounted for by an extension of Ruth's law in which the filtration time to filtrate volume ratio can be captured by the equation

$$\frac{t}{V} = \frac{\eta \kappa r_{\mathrm{c}} \frac{|\nabla B_{\mathrm{crit}}|M_{\mathrm{crit}} - |\nabla B|M}{|\nabla B_{\mathrm{crit}}|M_{\mathrm{crit}}}}{2A^2 \Delta p} V + \frac{\eta R_{\mathrm{m}}}{A \Delta p} \tag{10}$$

with the filtration area A.

To quantify the structure of a filter cake formed in the magnetic field an energy ratio E_{S} can be defined[1] similar to the energy ratio for magnetically stabilized fluidized beds suggested in Ref. 28.

$$E_{\mathrm{S}} = \frac{E_{\mathrm{hyd}}}{E_{\mathrm{m,dip}}} = \frac{3\pi\eta d^2 v}{\frac{1}{144}\pi\mu_0\rho_{\mathrm{s}}^2 M^2 d^3} = \frac{432\eta v}{\mu_0 \rho_s^2 M^2 d} \tag{11}$$

The hydrodynamic drag potential E_{hyd} defines the energy that is needed to lift one particle against the drag force F_{hyd} by one particle diameter (Eq. 2). This potential describes the hindrance to the formation of the magnetically induced particle configuration due to the flow of the liquid phase. The magnetic dipole energy $E_{\mathrm{m,dip}}$ is the repulsive energy between two particles in contact perpendicular to the external field direction (Eq. 6). For $E_{\mathrm{S}} < 1$ the structure is strongly ordered, for $1 < E_{\mathrm{S}} < 10$ a partly structured and for $E_{\mathrm{S}} > 10$ an unstructured bed can be assumed. This parameter serves as a convenient metric to compare the regimes of experimental and calculated results.

DEM-Simulation

DEM

The DEM is an approach for solving Newton's laws of motion for all N discrete elements allowing for all degrees of freedom to describe the motion of each particle individually in the system depending on time t:

$$m_{\mathrm{i}} \frac{d\vec{v}_{\mathrm{i}}}{dt} = \vec{F}_{\mathrm{i}} \tag{12}$$

$$I_{\mathrm{i}} \frac{d\vec{\omega}_{\mathrm{i}}}{dt} = \vec{T}_{\mathrm{i}} \tag{13}$$

where v_{i}, ω_{i}, m_{i}, I_{i} are, respectively, the transitional velocity, rotational velocity, mass, and moment of inertia of particle i. The force vector $\vec{F}_{\mathrm{i}}$ is composed of the different external and interaction forces explained earlier and contact forces in normal ($F_{\mathrm{n,ij}}$) and tangential ($F_{\mathrm{t,ij}}$) direction acting on sphere i:

$$\vec{F}_{\mathrm{i}} = \sum (\vec{F}_{\mathrm{el,ij}} + \vec{F}_{\mathrm{vdW,ij}} + \vec{F}_{\mathrm{m,dip,ij}} + \vec{F}_{\mathrm{n,ij}} + \vec{F}_{\mathrm{t,ij}}) + \vec{F}_{\mathrm{g,b}} + \vec{F}_{\mathrm{hyd}} + \vec{F}_{\mathrm{m,ext}} \tag{14}$$

Rotation phenomena ($\vec{T}_{\mathrm{i}}$) were not considered since the oriented magnetic field reduces the tendency of the particles to rotate. Consistent with the experimentally used particle systems, all elements were assumed to be regular spheres.[1]

Very stable and effective integration predictor-corrector methods[29,30] were implemented in the integration of Eqs. 12 and 13 to simulate granular particle systems, with the time step selected such that constant forces could be assumed within each iteration step.

Contact forces

Particle–particle contacts can be accounted for using either a hard-sphere approximation or the soft-sphere approach.[10,11] The hard-sphere assumption allows for fast simulations, and is suitable for dilute systems as it only considers binary collisions in a chronological order, with post-impact conditions calculated according to the Hertz contact theory.[31] In this work, however, the more useful soft-sphere approach was used in which multibody collisions are described in terms of a virtual overlapping of the spheres. These collisions were not calculated integrally but tracked differentially over the entire time step, enabling several contacts of one particle to be treated at the same time. The deformation of the spheres during collisions was replaced by a virtual overlap or deformation distance λ for the particles (Figure 1). This necessitates a set of reset forces in the normal and tangential directions from which follow different kinds of contact models.[11,13,32] The overlap was calculated from the particle diameters and the center-to-center distance between the particles according to

$$\lambda = \frac{d_{\mathrm{i}} + d_{\mathrm{j}}}{2} - |\vec{r}_{\mathrm{ij}}| \tag{15}$$

The contact forces during such collisions were modeled in terms of a series of spring elements, dampers, and sliders, as shown in Figure 2. The normal contact force

$$\vec{F}_{\mathrm{n,ij}} = k_n \lambda^{1,5} \vec{n}_{\mathrm{ij}} - \eta_{\mathrm{n,ij}} \vec{v}_{\mathrm{rel,n,ij}} \tag{16}$$

results from the parallel connection of a spring and a damping element characterizing the storage and dissipation of kinetic energy, respectively.[33] The normal vector connecting the center of particle i to that of particle j is given by $\vec{n}_{\mathrm{ij}}$.

The spring force, usually calculated by applying the Hertz contact theory for spheres, is a function of the spring stiffness and the virtual deformation of the spheres, which can be estimated using Young's modulus and Poisson's ratio. Often, the value of the spring stiffness calculated in this way does not reflect the true behavior adequately or the material properties are not known, and thus we used a different approach in which the stiffness was determined by an equilibrium between the maximum occurring force and the

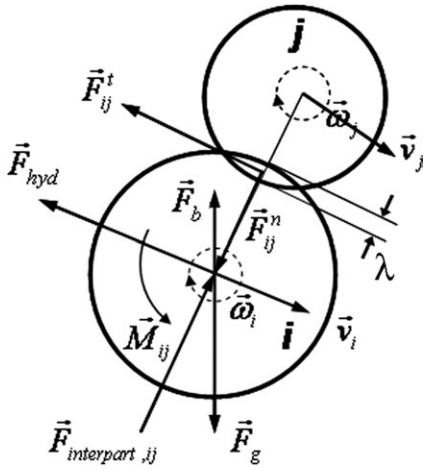

Figure 1. 2D description of the soft-sphere approach for the determination of force balances on particle–particle collision.

spring force allowed at a defined penetration λ^*.[11,34,35] Thus, the spring constant was calculated as

$$k_{\mathrm{n}} = \frac{|\vec{F}_{\max}|}{[d(1-\lambda^*)]^{1.5}} \tag{17}$$

The damping constant η_{n} was calculated from the particle mass m, the depth of overlap and the spring stiffness.[33] The damping coefficient is set to $c_{\mathrm{n}} = 0.3$.

$$\eta_{\mathrm{n,ij}} = c_{\mathrm{n}}\sqrt{\frac{9}{2}\left(\frac{m_{\mathrm{i}}m_{\mathrm{j}}}{m_{\mathrm{i}}+m_{\mathrm{j}}}\right)\sqrt{\lambda}k_{\mathrm{n}}} \tag{18}$$

In the tangential direction, the modus was similar with the only difference being that the static or dynamic friction coefficient $\mu_{\mathrm{stat/dyn}}$ was also incorporated in the spring constant:

$$k_{\mathrm{t,stat/dyn}} = \frac{\mu_{\mathrm{stat/dyn}}}{d(1-\lambda^*)}|\vec{F}_{\max}| \tag{19}$$

$$\eta_{\mathrm{t,ij}} = 2\sqrt{\frac{2}{7}\left(\frac{m_{\mathrm{i}}m_{\mathrm{j}}}{m_{\mathrm{i}}+m_{\mathrm{j}}}\right)k_{\mathrm{t,dyn}}} \tag{20}$$

In each iteration cycle, the Coulomb friction

$$|\vec{F}_{\mathrm{t,ij}}| \le \mu_{\mathrm{stat}}|\vec{F}_{\mathrm{n,ij}}| \tag{21}$$

was assessed to determine whether it must be allowed for or whether the particles slided over each other.

A relative tangential displacement $\Delta x_{\mathrm{t,ij}}$ of two particles in contact without the particles starting to slide results in an increase in the spring force via

$$\vec{F}_{\mathrm{t,ij}} = -k_{\mathrm{t,sta}}\Delta x_{\mathrm{t,ij}} - \eta_{\mathrm{t,ij}}v_{\mathrm{rel,t,ij}} \tag{22}$$

If the static friction is exceeded and the particles begin to move, the position and tangential forces are changed accordingly using the relations

$$\vec{F}_{\mathrm{t,ij}} = -\mu_{\mathrm{dyn}}|\vec{F}_{\mathrm{n,ij}}|\vec{t}_{\mathrm{ij}}\Delta x_{\mathrm{t,ij}} \tag{23}$$

$$\Delta x_{\mathrm{t,ij}} = -\frac{\vec{F}_{\mathrm{t,ij}}}{k_{\mathrm{t,dyn}}} \tag{24}$$

The efficiency of the numerical procedures was enhanced by calculating particle interactions only when particles were within a distance of three particle diameters of each other, assuming that particles do not interact beyond this distance. The determination of interacting particles was managed with a Verlet list.[36]

Cake build-up

Calculation of the filtrate velocity or the filtration resistance requires estimates of the height h_{c}, porosity ε and tortuosity τ of the filter cake. For this purpose, the simulation domain was divided into small cubic volume elements each with the feed size l, which was chosen arbitrarily, subject to the constraint that it should be larger than the particle diameter to avoid cells falling within a particle, which would lead to numerical instabilities. Each particle was prorated to one or more cells by geometric considerations. This approach enabled the full three-dimensional porosity profile of the entire simulation domain to be constructed, as well as the one-dimensional cross-sectional averaged profile with height. The cake height was defined in terms of a threshold value of the calculated porosity, since a distinct step in the lateral-averaged porosity exists between the free suspension and the filter cake.

The effective capillary length h_{eff} required for the estimation of the tortuosity (see Eq. 9) was estimated by determining a path through the filter cake following the highest porosity in each volume element of the cake, assuming this to be the main path of liquid flow with the lowest flow resistance. Allowing flow to the directly adjacent (number of cells: a) and diagonally conjunct cells ($\sqrt{2}b$,$\sqrt{3}c$), but suppressing a backward flow against the filtration resistance, we calculated the effective cake height using

$$h_{\mathrm{eff}} = \frac{l}{i}\sum_{\mathrm{i}}(a+\sqrt{2}b+\sqrt{3}c) \tag{25}$$

where i is the number of permeated cells. Finally, the filtration resistance was determined using Eq. 8 and the resulting liquid flow velocity calculated as a function of the cake height using Eq. 7.

Integration method

The third-order Adams-Bashforth-Moulton predictor-corrector integration algorithm[29] was used to calculate the particle positions and velocities at each time step while avoiding

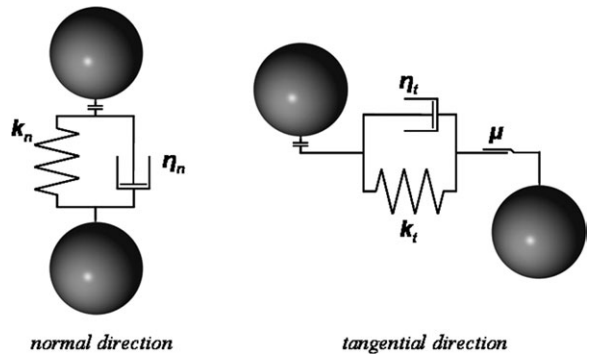

Figure 2. Particle contact model: spring and damper in normal direction; spring, damper and slider in tangential direction.

the implicit calculations of the Adams-Moulton approach. Although the approach for one-time step is implicit, due to the additional predictor step all calculations were executed explicitly using this method. The particle position x at any given time step Δt was determined using a weighted average of the results of the velocity v of the last two time steps, i.e.,

$$x_{n+1,\text{predictor}} = x_n + \frac{\Delta t}{12}(23v_n - 16v_{n-1} + 5v_{n-2}) \tag{26}$$

After calculating the new load case with the predicted particle coordinates and the new acceleration

$$a_n = \frac{6}{\pi d_\text{p}^3 \rho} \sum_\text{i} F_\text{i} \tag{27}$$

the velocity $v_{\text{n+1,corrector}}$ and position $x_{\text{n+1,corrector}}$ were updated in the corrector step within the same time step of the integration[37]:

$$v_{n+1,\text{corrector}} = v_n + \frac{\Delta t}{12}(5a_n + 8a_{n-1} - a_{n-2}) \tag{28}$$

$$v_{n+1,\text{corrector}} = x_n + \frac{\Delta t}{12}(5v_{n+1,\text{corrector}} + 8v_n - v_{n-1}) \tag{29}$$

Different time scales were used to reduce the computational effort in our studies. The time step in the integration of the equation of motion was chosen to be small to fulfill the requirement for constant forces during a given time step interval. The maximum time step was limited by the maximal force, i.e., the spring force during particle collision, which, in turn, depended on the penetration length λ^* and the mobility of the particle. Therefore, the time step was determined via

$$\Delta t = K \frac{3\pi\eta d}{F_\text{max}} \lambda^* \tag{30}$$

where the weighting factor was selected to be $K = 0.2$.[38]

Parameters that are less time and particle position sensitive, such as the Verlet list, the direction of the magnetic moments, and the filter cake properties (ε, h_c, τ) were updated less frequently using a larger time step.

Boundary Conditions and Material Parameters

Before the start of the simulation, particles were positioned randomly inside the simulation domain until the required solid volume fraction was reached. The same arbitrary initial orientation of the particles was used in all simulations. Gravity and hydrodynamic drag were assumed to act in the negative axial z-direction, while the magnetic field was taken to be uniform in the lateral x- and y-directions, but varied axially to establish a gradient in the magnetic flux density in z-direction that was responsible for the magnetic force opposing gravity and hydrodynamic drag forces.

The lower boundary of the simulation domain was confined by the filter medium with a defined permeability for the aqueous phase only. The contact between the filter medium and a particle was treated as a particle-wall collision using the same spring constant as used for particle–particle collisions with the filter medium mass set to infinity. A high tangential spring constant inhibited particle sliding on the filter medium. The upper limit to the simulation domain was defined by the liquid surface, which decreased with time as the liquid volume diminished during filtration. All sides parallel to the z-axis of the simulation domain were treated as periodic boundaries. Initial values for filtration pressure, filter medium resistance, magnetic field strength and material properties were chosen to be consistent with experimental parameters used in previous studies.[1] Only the magnetic flux density B was varied between simulation runs. The parameters are summarized in Table 1.

Table 1. Physical Conditions and Numerical Parameter Values

Name	Value	Reference
Particle diameter d_p/m	5×10^{-6}	Particle properties of PVAc magnetic beads[1]
Solid density ρ_s/kg/m^3	1400	
Zeta potential ζ/V	-5×10^{-3}	
Saturation magn. M_S/A m^2/kg	22.6	
Remanent magn. M_R/A m^2/kg	0	
Static friction coeff. μ_stat/–	0.075	Experiments with magnetic analyzing centrifuge[7]
Sliding friction coeff. μ_dyn/–	0.025	
Hamaker constant H_o/J	10^{-20}	Ref. 21
Contact distance a_p/m	10^{-9}	Ref. 12
Liquid density ρ_l/kg/m^3	1000	Physical properties of water
Viscosity η/Pa·s	10^{-3}	
Ion concentration c/mol/l	10^{-7}	
Filter cloth resistance R_m/m^{-1}	10^9	Estimation based on experimental data[1]
Temperature T/°C	25	Experiments with Nutsche filter[1]
Solid concentration c_v/–	0.095	
Differential pressure Δp/Pa	60,000	
Magnetic flux density B/T	0…0.1	
Gradient ∇B/T/m	0…3.82	
Number of particles N/–	700	
Width of simulation area x/m	4×10^{-5}	
Depth of simulation area y/m	4×10^{-5}	
Height of simulation area z/m	10^{-4}	
Penetration length λ^*/m	$0.985 \cdot d_\text{p}$	
Time step $\Delta t_{\text{particle contact}}$/s	10^{-6}	Estimation based on Eq. 30
Time step $\Delta t_{\text{filtration, agglomeration}}$/s	10^{-4}	

Results and Discussion

Particle agglomeration in the suspension

With increasing field strength the range and magnitude of the magnetic dipole interactions increase, inducing the formation of larger stable agglomerates. The formation of the agglomerates is evident in the snapshots in Figure 3, which shows the state of the particles in the free suspension after $t = 0.1$s. In the absence of the magnetic field, and hence of long-range interactions, the particles retained their initial positions relative to each other (Figure 3a), but with even weak magnetic fields (e.g., $B = 0.01$T) the particles moved relative to each other and began to orient in the field direction (Figure 3b). With increasing field strength the particles interacted more strongly and formed chains in the direction of the magnetic field (Figure 3c, d). In addition to increasing in size, the agglomerates also adopted a less tortuous configuration in the magnetic field direction.

The length of (i.e., the number of particles in) the particle chains was determined for each of the conditions studied, and the distribution in the normalized agglomerate or

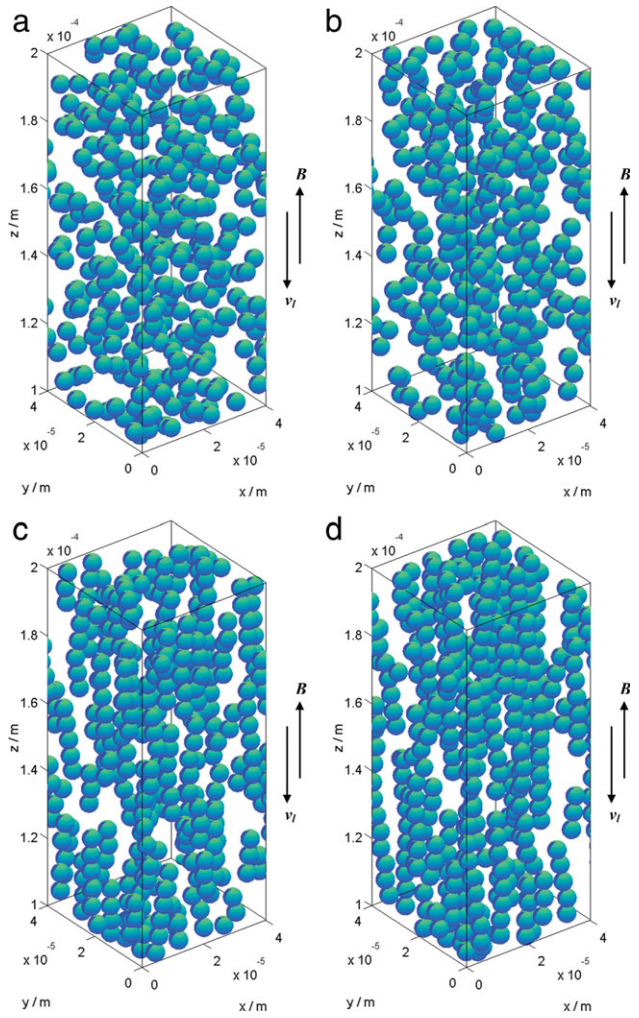

Figure 3. Snapshots of the upper half of the simulation area after t = 0.1s for different magnetic flux densities (B = 0...0.07T) showing agglomerate formation in the free suspension due to magnetic dipole interactions.

(a) B = 0T (b) B = 0.01T, (c) B = 0.05T, and (d) B = 0.07T. [Color figure can be viewed in the online issue, which is available at wileyonlinelibrary.com.]

particle chain size is given as a function of the applied magnetic flux density in Figure 4. At each field strength, a wide distribution in agglomerate sizes was observed. The average chain length approached an upper limit with increasing magnetic field strength as the particles became saturated magnetically and no further increase in dipole-dipole interactions was possible with increasing field strength. Following the initial growth of chains or agglomerates the size distribution attained a steady, unchanging value. Thus, the porosity, tortuosity and cake resistance could be assumed to be constant during the subsequent simulations.

The external magnetic force should also be taken into account since it acts in a direction opposite to the gravitational and hydrodynamic drag forces and hence retards the particle movement in the axial direction. According to Equation 3, the external magnetic force increases with increasing field strength and agglomerate size such that even for a flux density of B = 0.1T the external magnetic force is sufficiently strong to initiate particle movement in the direction of the magnetic field gradient. In the beginning of the simulation, single particles and smaller agglomerates still followed the liquid flow until they were trapped by or appended to larger agglomerates. Under these conditions, the particles accumulated at the liquid surface as shown in Figure 5, which is represented by the thin grid in the snapshots. Since surface effects were not implemented in the simulation, this state cannot be analyzed in detail, but it is important to note that this state of an avoided cake build-up and an open or free filtration area is consistent with experimental observations.[1]

Structuring effects in the filter cake

The chains observed in the suspension were also found in the filter cake, with structure development as shown in the snapshots of the filter cake at the end of the cake build-up period for different magnetic field strengths given in Figure 6. Without the magnetic field, the particles formed an irregular packed bed on top of the filter medium (z = 0m) (Figure 6a). Because of hydrodynamic forces and the framework pressure inside the filter cake this compacting was also observed at low flux densities (Figure 6b). Only at the cake surface where the load on the particles is lower than inside could some particles stabilized by the magnetic dipole forces be detected. Finally, with higher flux densities the structure became stable. For a flux density of B = 0.05T, for instance, two different regimes could be identified in the filter cake (Figure 6c), with the lower portions of the filter cake still compacted due to the higher framework pressure, although some retention of the original needle-like structure not seen under lower field strengths was evident. In the upper portions, the chained structure was even more stable, and the cake possessed a higher porosity and lower tortuosity than observed for lower magnetic field strengths. In addition, agglomerates of several chains occured, since due to the lower distances the attractive forces between the chains sufficed to initiate further aggregation. For B = 0.07T, the magnetically-induced chain structure was maintained over the whole cake height (Figure 6d). It can be inferred from the change in the structure of the packed bed that the application of the magnetic field will have an effect on both the porosity and the tortuosity of the flow channels, as discussed in more detail given below.

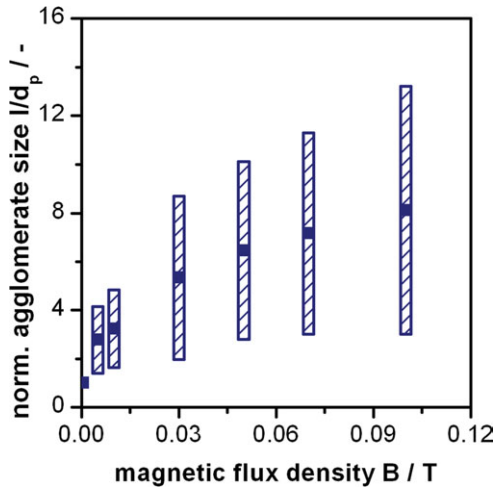

Figure 4. Normalized agglomerate size as a function of the magnetic flux density after t = 0.1s.

Striped bar: size range; solid square: average size. [Color figure can be viewed in the online issue, which is available at wileyonlinelibrary. com.]

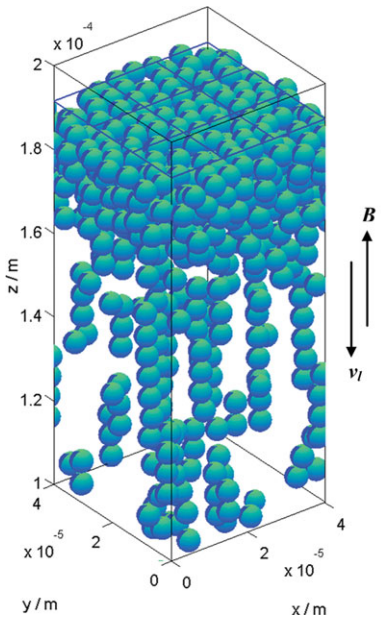

Figure 5. Snapshot of the upper half of the simulation area after $t = 0.1$s for $B = 0.1$T showing the accumulation of the particles at the liquid surface.

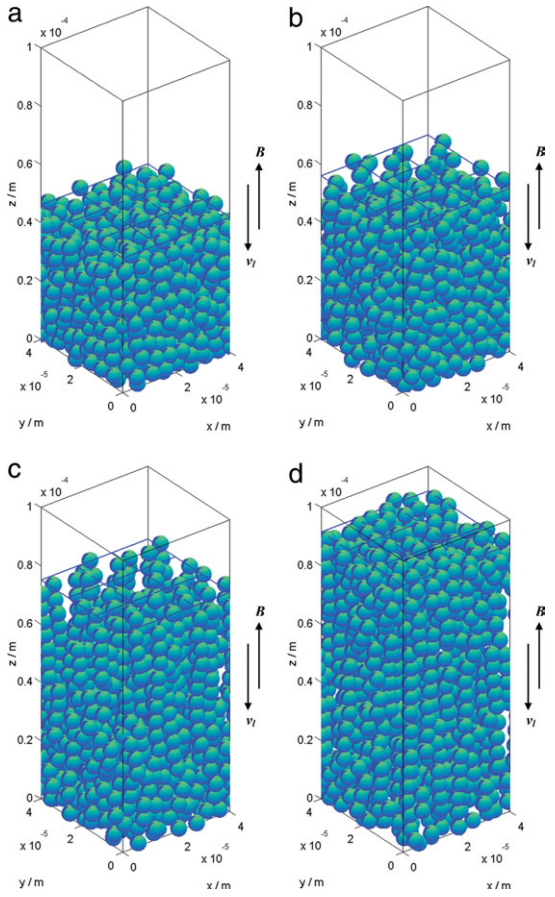

Figure 6. Snapshots of the filter cakes at the end of the cake building period for different magnetic flux densities ($B = 0...0.07$T) showing the change in the cake structure due to the superposed magnetic field.

(a) $B = 0$T (b) $B = 0.01$T, (c) $B = 0.05$T, and (d) $B = 0.07$T. [Color figure can be viewed in the online issue, which is available at wileyonlinelibrary.com.]

The filtration velocity is a common and usually a practical parameter for charactering any given filtration process, and generally decreases strongly with increasing filtration time and/or cake height. In our simulations, the low simulated cake heights did not provide a significant resistance to flow, and thus filtration velocity was not a sensitive enough measure of the progress of the filtration process. Instead, we characterized the effects of magnetic fields on the filtration process by reporting their influence on other, more sensitive parameters such as bed height, porosity and tortuosity. Figure 7, for instance, presents the increase in cake height with filtration time for different magnetic flux densities. At low flux densities, the trend is very much the same as for classical cake filtration processes, where, although the cake height increased with time due to an increasing cake porosity, the lower layer of the filter cake was still compacted and the overall filtration resistance was changed only slightly. In general, the results for $B \leq 0.01$T correspond to the classical curve for cake build-up, where the filtration, and hence change in cake height, is rapid in the early stages of the process, but slows down as the resistance builds up. Deviations from this behavior occurred for $B = 0.03$T and higher. Initially, the cake height was lower in the presence of a magnetic field than in its absence, because the hydrodynamic drag forces were counteracted by the magnetic forces, and hence the particle migration to the filter medium was reduced; this is the reason for the apparent lag in the start of the cake formation, particularly at high magnetic flux densities. Once the build-up began, however, it grew at a faster pace than in the nonmagnetic system owing to the lower resistance to flow afforded by the cake. At some point, however, the cake height became larger than in the nonmagnetic system because the filtration ran more quickly due to the reduced resistance offered by the more structured cake. This behavior intensified with increasing flux density. Thus, the cake height increased more rapidly with $B = 0.07$T than at lower magnetic field strengths. The critical flux density was reached at $B = 0.1$T where the upward magnetic forces on the particles just balanced the downward forces due to hydrodynamic drag and gravity, so that the particles were

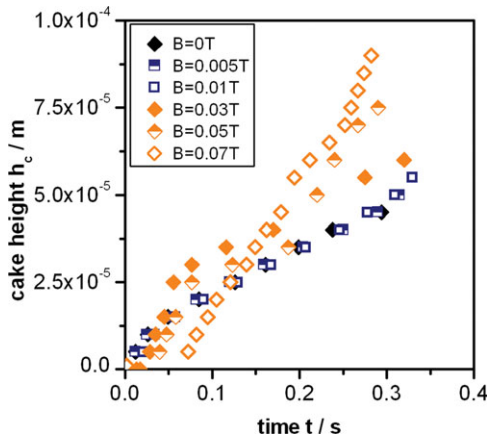

Figure 7. Cake height as function of filtration time for different magnetic flux densities ($B = 0...0.01$T).

[Color figure can be viewed in the online issue, which is available at wileyonlinelibrary.com.]

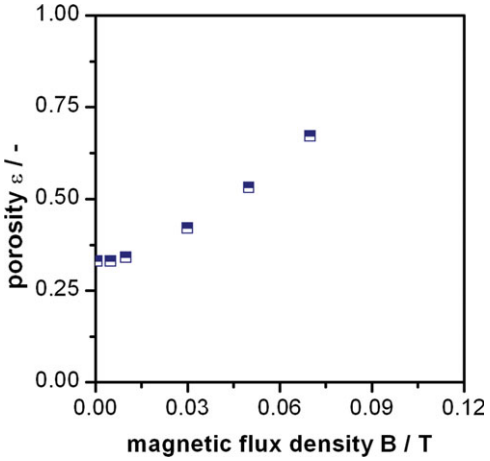

Figure 8. Filter cake porosity as function of the magnetic flux density *B*.

[Color figure can be viewed in the online issue, which is available at wileyonlinelibrary.com.]

unable to reach the filter medium and no cake build-up occurred.

As is evident from the snapshots in Figure 6, changes in magnetic field strength resulted in structural changes in the filter cake itself, and thus strongly influenced the magnitude and position-dependence of the porosity and the tortuosity within the cake. Figures 8 and 9 show the variations of these parameters averaged over the cake height with increasing magnetic flux density the porosity of the cake obtained in classical filtration was $\varepsilon = 0.33$ and lay in a realistic range for cake porosities of such particle systems (Figure 8). Because of the magnetic dipole forces the porosity increased strongly under applied magnetic fields, in the present case up to $\varepsilon = 0.72$ for $B = 0.07$T. For simulations with more particles, i.e., higher cake heights, the average porosity would reach a limit, or at least not increase as rapidly, due to increases in the framework pressure with a consequent compaction of the structure. This consolidation occurred especially on the lower part of the filter cake. To identify the gradient of the particle load over the filter cake height a contact force network, such as applied in Ref. 12 could be drawn. It is expected that the change from the horizontally isotropic cake structure in classical filtration to the anisotropic, needlelike structure could visualized. To reflect accurately the contact force gradient over the cake height the simulation must consist of a larger number of particles. Thus, this method of display will be adopted in future work.

Figure 9 shows that tortuosity decreases with increasing magnetic flux density. The range of tortuosity values (bars showing distribution) was due to the small cake heights; it would be narrower for larger cake heights. Without the magnetic field the values were in the region $\tau = 1.5$, consistent with the theoretical value predicted by Carman and Kozeny of $\tau = \sqrt{2}$.[27] At higher magnetic flux densities, the tortuosity decreased as the pore geometry became straighter, and approached $\tau = 1$ at very high field strengths. This porosity value of unity corresponds to a parallel capillary system with totally straight pores, comparable with the model of an ideal columnar structure derived from the experimental results.[1] Practically, however, the critical field strength was exceeded, preventing the cake build-up before this columnar state was reached.

Finally, with the porosities and tortuosities determined above, the cake resistance was calculated using Eq. 8 and reported in Figure 10. As in the experiments, the value $r_c = 10^{14}$ m^{-2} indicates poor filtration performance in the absence of a superposed magnetic field. This performance was improved with increasing field strength as indicated by the continuing reduction in cake resistance until the critical flux density is reached. Two different regions can be indicated. For low magnetic flux densities, the external magnetic force is relatively weak, although a strong dependency on the magnetic flux density was observed. Since external magnetic forces are weak for these low flux densities, the change in the cake resistance can be attributed to the change in the cake structure. Once the maximum structuring had been reached, the external magnetic force led to an additional lowering of the resistance. This additional reduction was less than the structuring contribution, however, as reflected in its lower dependency on the actual field strength.

Comparison with experimental results

Comparisons can be drawn between the modeling results presented here and the experimental results published earlier.[1] The simulated filter cake resistance of $r_c = 1.04 \times 10^{14}$ m^{-2}

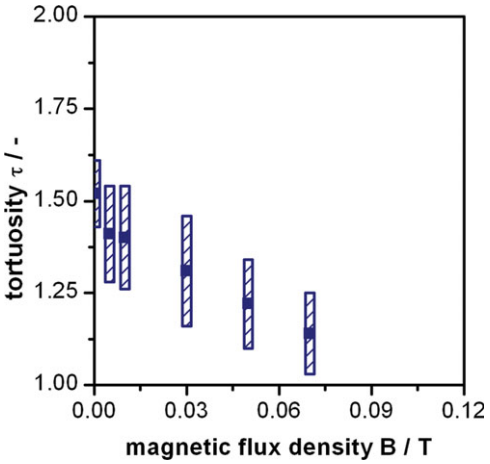

Figure 9. Tortuosity as function of the magnetic flux density *B*.

[Color figure can be viewed in the online issue, which is available at wileyonlinelibrary.com.]

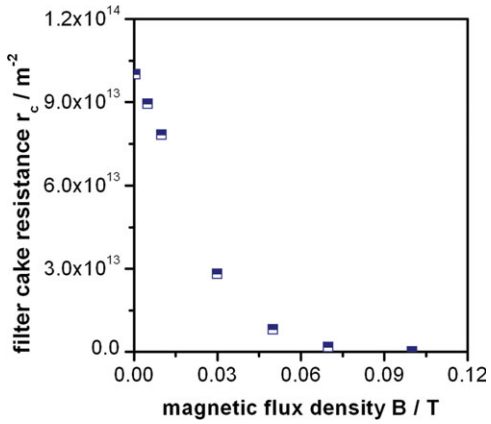

Figure 10. Filter cake resistance as a function of the magnetic flux density *B*.

[Color figure can be viewed in the online issue, which is available at wileyonlinelibrary.com.]

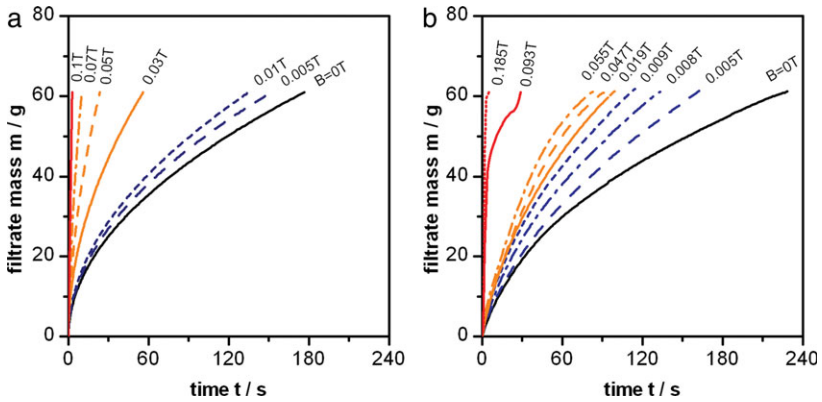

Figure 11. Simulated (left) and experimental (right) filtration curves for different magnetic flux densities *B*.

[Color figure can be viewed in the online issue, which is available at wileyonlinelibrary.com.]

compared favorably with the value of $r_c = 0.82 \times 10^{14}$ m^{-2} determined experimentally for the classical filtration case, and the predicted and experimental critical flux densities B_{crit} also agreed well ($B_{crit,sim} = 0.1$T; $B_{crit,exp} = 0.098$T). For intermediate flux densities, good qualitative agreement was obtained, with similar distinction between the two regions of magnetic field influence, as shown in Figure 11. The filtrate curves were calculated using Eq. 10, incorporating the simulated cake resistance and the critical magnetic flux density. Since the simulations only covered a small operating region of a real filtration process, the curves were extrapolated to reflect the same filtrate mass and filtration area conditions as used in the experiments.

Although the parameters for the simulation were chosen to be similar to those used in the experiments, there are some major differences that led to deviations between the two sets of results. The number of particles in the experiments can be estimated to be $N \approx 10^{10}$, while the simulations only allowed for $N = 700$ particles. This immense scale-up factor could have led to significant discrepancies between the filtration curves, but the differences over the actual simulated region are small. The reasons for these anticipated discrepancies are that the simulated filter cake was incorrectly taken to be incompressible over the scale-up range, and that the particles were monodisperse; both assumptions are unrealistic. Thus, the simulated filtration rate was too fast compared to the experiments, although good qualitative agreement between the two was achieved.

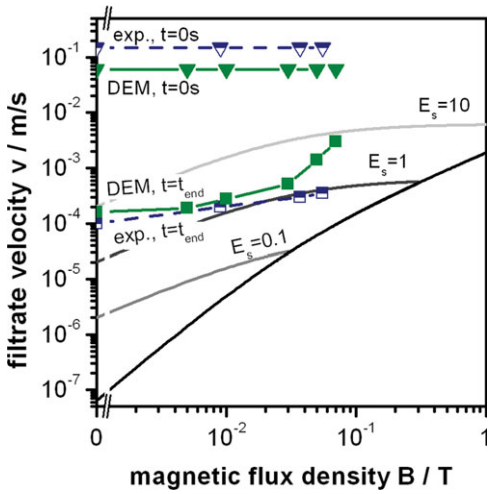

Figure 12. Phase diagram of different structural regions as function of filtrate velocity v and magnetic flux density *B*.

[Color figure can be viewed in the online issue, which is available at wileyonlinelibrary.com.]

Figure 12 provides a phase diagram of the cake structure based on the structuring parameter E_S, which enables a qualitative comparison between the simulated and experimental results to be made. The magnetic flux density and the filtrate velocity ranges shown span an operational range over which the filter cake structure varies, partitioned by several curves of constant structuring parameter (according to Eq. 11). The region without cake build-up (lower right-hand corner, below the solid black curve) allows the critical flux density to be identified. The trajectory of a given filtration run can be followed along a vertical line at a constant magnetic flux density starting at a high filtrate velocity in the region of high structuring parameters, i.e., low structuring effects in the packed bed. With increasing cake height, the velocity reduces and the hydrodynamic stress on the particles is lower. As a consequence, the state moves to a region of lower values for E_S, i.e., higher structuring, until the end velocity (at t_{end}) is reached beyond which the liquid flow diminishes.

With higher field strength it is observed, that E_S is reduced further even with increasing filtrate velocity. This indicates that the higher magnetic interactions are able to stabilize the structure against the hydrodynamic stress. Both the experimental and the simulated results indicate that with increasing magnetic flux density E_S decreases while the final filtration velocity increases. This seems to be more prominent for the simulated system, attributed to the fact that the filter cake was assumed not to be compressible and the structuring effect was slightly overestimated.

Conclusions

The DEM-simulations of magnetically-enhanced cake filtration presented capture the overall experimentally-observed trends on filtration velocity variations with time under different applied magnetic fields. The results provide strong insight into the mechanisms of the magnetic field enhanced filter cake structuring and confirm the hypothesis derived from experiments that, especially at low field strengths, the change in permeability of the filter cake due to magnetic dipole-dipole interactions improves filtration performance. To study the particle load in detail contact force networks

over the filter cake height will be adopted. The qualitative agreement between the simulations and reported experimental results on the dependency of the cake properties and filtration performance on the applied magnetic field strength provides conformation of the basic assumptions inherent in the model. In future work, the effect of the resistance of particles against rolling and sliding should be incorporated in the model. Further enhancements to the model, such as a material properties depending spring constant, inclusion of hydrodynamic interactions and particle or agglomerate rotation coupled with a larger number of particles, should provide more quantitative predictions of the performance of magnetically-enhanced cake performance, which in turn could be useful for the evaluation and design of new magnetically-enhanced separation strategies.

Acknowledgments

This work results from cooperation between the Karlsruhe Institute of Technology, Germany, and the Massachusetts Institute of Technology, USA. CE thanks the Karlsruhe House of Young Scientists (KHYS) of the Karlsruhe Institute of Technology for financial support.

Notation

Symbols

$\vec{m}$ = direction vector of magnetic moment
$\vec{n}$ = normal vector
$\vec{t}$ = tangential vector
a = acceleration ($m \cdot s^{-2}$)
a = counting number in Eq. 25
a = distance (m)
A = filtration area (m^2)
b = counting number in Eq. 25
B = magnetic flux density, scalar (T)
c = concentration ($mol \cdot l^{-1}$)
c = counting number in Eq. 25
c_n = damping coefficient in Eq. 18
d = diameter (m)
E = energy (J)
e_0 = elementary charge = $1.6021 \cdot 10^{-19}$ C
E_S = structure parameter
F = force (N)
g = gravitational acceleration = 9.81 $m \cdot s^{-2}$
h = height (m)
H_0 = Hamaker constant (J)
i = counting number in Eq. 25
k = Boltzmann constant = $1.3806 \cdot 10^{-23}$ $J \cdot K^{-1}$
K = weighing factor in Eq. 30
k_0 = form factor in Eq. 8 = 2.5
l = length (m)
M = magnetization ($A \cdot m^2 \cdot s^{-1}$)
N = particle number
N_A = Avogadro number = $6.02214 \cdot 10^{23}$ mol^{-1}
P = permeability (m^2)
p = pressure (Pa)
r = distance (m)
r = specific resistance (m^{-2})
R_m = filter media resistance (m^{-1})
T = temperature (K)
t = time (s)
v = velocity ($m \cdot s^{-1}$)
v_∞ = background velocity ($m \cdot s^{-1}$)
V = volume (m^3)
x = position (m)
y = position (m)
z = position (m)
z = valence number
γ = factor in Eq. 14
ε = permittivity ($A \cdot s \cdot V^{-1} \cdot m^{-1}$)
ε = porosity
ε_0 = permittivity of vacuum = $8.8542 \cdot 10^{-12}$ $A \cdot s \cdot V^{-1} \cdot m^{-1}$
ζ = zeta potential (V)
η = damping coefficient (s^{-1})
η = dynamic viscosity (Pa·s)
κ = concentration parameter
κ = reciprocal Debye length (m^{-1})
λ = penetration length (m)
μ_0 = magnetic permeability of vacuum = $4 \cdot \pi \cdot 10^{-7}$ $V \cdot s \cdot A^{-1} \cdot m^{-1}$
ρ = density ($kg \cdot m^{-3}$)
τ = tortuosity
χ = magnetic susceptibility

Indices

∞ = background
b = buoyancy
c = cake
$crit$ = critical
dip = dipole
eff = effective
el = electrostatic
end = end of the experiment/ simulation
exp = experimental
ext = external
g = gravity
hyd = hydrodynamic
i = counting index
j = counting index
l = liquid
m = magnetic
max = maximum
n = counting index in Eqs. 26–29
n = normal
r = relative
rel = relative
s = solid
sim = simulated
t = tangential
vdW = van der Waals

Literature Cited

1. Eichholz C, Stolarski M, Goertz V, Nirschl H. Magnetic field enhanced cake filtration of superparamagnetic PVAc-particles. *Chem Eng Sci*. 2008;63:3193–3200.
2. Svarovsky L. *Solid-liquid Separation. Butterworths Monographs in Chemistry and Chemical Engineering*, 2nd ed. London, UK: Butterworth, 1981.
3. Fuchs B, Stolarski M, Stahl W, Nirschl H. Magnetic field enhanced cake filtration. *Filtration Solutions*. 2006;6:333–339.
4. Charles S. Aggregation in magnetic fluids and magnetic fluid composites. *Chem Eng Commun*. 1988;67:145–180.
5. Chin CJ, Yiacoumi S, Tsouris C, Relle S, Grant SB. Secondary-minimum aggregation of superparamagnetic colloidal particles. *Langmuir*. 2000;16:3641–3650.
6. Stolarski M, Fuchs B, Bogale S, Eichholz C, Nirschl H. Magnetic field enhanced press-filtration. *Chem Eng Sci*. 2006;61:6395–6403.
7. Eichholz C. *Zur Magnetfeldinduzierten Strukturierung von Filterkuchen - Experimenteller Nachweis, Simulation und Anwendung in der selektiven Bioseparation*. Göttingen, Germany: Cuvillier Verlag, 2010.
8. Cundall, PA, Strack ODL. Discrete numerical-model for granular assemblies. *Geotechnique*. 1979;29:47–65.
9. Chen JC, Kim AS. Brownian dynamics, molecular dynamics, and Monte Carlo modeling of colloidal systems. *Adv Colloid Interface Sci*. 2004;112:159–173.
10. Johnson KL. *Contact Mechanics* (9th edition). Cambridge, UK: Cambridge University Press, 1985.
11. Deen NG, Annaland MV, Van der Hoef MA, Kuipers JAM. Review of discrete particle modeling of fluidized beds. *Chemical Engineering Science*. 2007;62(1–2):28–44.
12. Dong KJ, Zou RP, Yang RY, Yu AB, Roach G. DEM simulation of cake formation in sedimentation and filtration. *Miner Eng*. 2009;22: 921–930.
13. Zhu HP, Zhou ZY, Yang RY, Yu AB. Discrete particle simulation of particulate systems: theoretical developments. *Chem Eng Sci*. 2007;62:3378–3396.
14. Marshall J. Discrete-element modelling of particulate aerosol flows. *J Comput Phys*. 2009;228:1541–1561.
15. Deryagin B, Landau L. Acta Physicochimica. *URSS*. 1941;14:633.
16. Verwey E, Overbeek J. *Theory of the Stability of Lyophobic Colloids*. New York: Elsevier, 1948.

17. Chin CJ, Yiacoumi S, Tsouris C. Probing DLVO forces using interparticle magnetic forces: Transition from secondary-minimum to primary-minimum aggregation. *Langmuir*. 2001;17:6065–6071.
18. Stolarski M, Eichholz C, Fuchs B, Nirschl H. Sedimentation acceleration of remanent iron oxide by magnetic flocculation. *China Particuology*. 2007;5:145–150.
19. Gregory J. Interaction of unequal double-layers at constant charge. *J Colloid Interface Sci*. 1975;51:44–51.
20. Hamaker HC. The London-van der Waals attraction between spherical particles. *Physica IV*. 1937;10:1058–1072.
21. Lagaly G, Schulz O, Zimehl R. *Dispersionen und Emulsionen*. Darmstadt, GER: Dr. Dietrich Steinkopff Verlag, 1997.
22. Kim AS, Hoek EMV. Cake structure in dead-end membrane filtration: Monte Carlo simulations. *Environ Eng Sci*. 2002;19:373–386.
23. Svoboda J. *Magnetic Techniques for the Treatment of Materials*. Amsterdam, NL: Elsevier Sc. Publishers, 1987.
24. Satoh A, Chantrell RW, Coverdale GN, Kamiyama S. Stokesian dynamics simulations of ferromagnetic colloidal dispersions in a simple shear flow. *J Colloid Interface Sci*. 1998;203:233–248.
25. Chen F. Magnetically enhanced centrifugation for continuous biopharmaceutical processing. Massachusetts Institute of Technology: Thesis (Ph.D.), 2009.
26. Ruth B, Montillon G, Montonna R. Studies in filtration - II. Fundamental axiom of constant-pressure filtration. *Ind Eng Chem*. 1933; 25:153–161.
27. Sorrentino, J. *Advances in Correlating Filter Cake Properties with Particle Collective Characteristics*. Aachen, Germany: Shaker-Verlag, 2002.
28. Rosensweig R, Jerauld G, Zahn M. *Structure of magnetically stabilized fluidized solids. Conference of Continuum Models of Discrete Systems*. Stockholm, Sweden, Vol. 4, (1981), 137–144.
29. Kruggel-Emden H, Sturm M, Wirtz S, Scherer V. Selection of an appropriate time integration scheme for the discrete element method (DEM). *Comp Chem Eng*. 2008;32:2263–2279.
30. Gear CW. *Numerical Initial Value Problems in Ordinary Differential Equations*, 7th ed. Englewood Cliffs: Prentice-Hall Inc., 1971.
31. Hertz H. Über die Berührung fester elastischer Körper. *Journal für die reine und angewandte Mathematik*. 1881;171:156–171.
32. Antonyuk S, Heinrich S, Tomas J, Deen N, van Buijtenen M. Energy adsorption during compression and impact of dry elastic-plastic spherical granules. *Granular Matter*. 2010;12:15–47.
33. Chu KW, Yu AB. Numerical simulation of complex particle-fluid flows. *Powder Technol*. 2008;179:104–114.
34. Langston PA, Tuzun U, Heyes DM. Discrete element simulation of granular flow in 2d and 3d hoppers - dependence of discharge rate and wall stress on particle interactions. *Chem Eng Sci*. 1995;50:967–987.
35. Simsek E, Wirtz S, Scherer V, Kruggel-Emden H, Grochowski R, Walzel P. An experimental and numerical study of transversal dispersion of granular material on a vibrating conveyor. *Particulate Sci Technol*. 2008;26:177–196.
36. Frenkel D, Smit B. *Understanding molecular simulation: from algorithms to applications. Computational Science Series*, 2nd ed. San Diego: Academic Press, 2002.
37. Beeman D. Some multistep methods for use in molecular-dynamics calculations. *J Comput Phys*. 1976;20:130–139.
38. Mishra B, Murty C. On the determination of contact parameters for realistic DEM simulations of ball mills. *Powder Technol*. 2001; 115:290–297.

Manuscript received July 5, 2011, revision received Nov. 15, 2011, and final revision received Jan. 23, 2012.